Denoising surface waves extracted from ambient noise using three-station interferometry: Methodology and application to 1-D linear array

Hongrui Qiu[1], Fenglin Niu[1], and Lei Qin[2]

[1]Department of Earth, Environmental and Planetary Sciences, Rice University, Houston, TX, USA

[2] Department of Earth Sciences, University of Southern California, Los Angeles, CA, USA

Corresponding author: Hongrui Qiu (hq7@rice.edu; qiuhonrui@gmail.com)

Key points:

- Surface waves from ambient noise cross correlations are significantly enhanced at high frequencies using three-station interferometry
- Phase travel times are extracted reliably between 0.3-1.6 s for a 1.6-km-long linear array and are used to perform surface wave tomography
- Phase velocity models of Rayleigh and Love waves derived via eikonal tomography reveal high-resolution fault zone images

Abstract

We develop an automatic workflow for denoising the fundamental mode surface wave from ambient noise cross correlations (ANCs) calculated for a dense linear array. The surface wave signal traveling between each station pair is first enhanced through three-station interferometry. Then, phase travel times at different periods are determined in the frequency domain. The proposed array-based method is applied to a 1.6-km-long dense linear nodal array crossing surface traces of the San Jacinto fault near Anza, California. Surface wave signals in ANCs of the nodal array are significantly enhanced after denoising, particularly at high frequencies (> 2 Hz). Phase travel times are extracted reliably in the period ranges of 0.3-1.3 s and 0.3-1.6 s for Rayleigh and Love waves, respectively. The corresponding period-dependent phase velocity profiles derived from the eikonal equation reveal high-resolution details of fault zone internal structures beneath the array. A broad (500-1000 m) low-velocity zone that narrows with increasing period is observed, illuminating a flower-shaped structure of the San Jacinto fault damage zone.

Plain Language Summary

Properties of fault damage zone (width of 100-1000's meters), such as its geometry and velocity reduction compared to the surrounding host rock, can have a profound impact on our understandings of earthquake ruptures and the long-term behavior of the fault. Several dense nodal arrays with 10-100 m spacing and aperture of a few kilometers were deployed crossing surface traces of major faults, to provide high-resolution images of the fault zone internal structures. Surface waves propagate between every two sensors with frequency-dependent speeds are extracted from ambient noise cross correlations. By measuring the relation between velocity and frequency, we can infer structures at depth as surface waves are more sensitive to shallow structures at a higher frequency. However, surface waves extracted from ambient noise at high frequencies (> 2 Hz) that are essential to image fault zone in the top 100's meters are often very noisy. Here, we develop a new method that utilizes three-station interferometry to suppress signals that are not traveling on the surface. The quality of surface waves is significantly improved after the denoising,

especially at high frequencies (> 2 Hz), providing more reliable measurements and better constraints on fault zone internal structures at shallow depth.

1. Introduction

Noise-based surface wave tomography has been widely used to resolve crustal structures at various scales (e.g., Lin et al., 2009; Qiu et al., 2019; Wang et al., 2019; Zigone et al., 2019). Analysis of high frequency (e.g., > 1 Hz) surface waves provides crucial information on the shallow (top 10s to 100s of meters) materials with unprecedented spatial resolution and thus improves our understanding of the local seismic hazard. In contrast to high-quality signals at long periods (e.g., > 2 s), extraction of surface waves from ambient noise cross correlations (ANCs) calculated at high frequencies (e.g., > 1 Hz) remains a challenging topic due to its low signal to noise ratio (SNR). Previous studies that utilize ANCs at high frequencies must first enhance the surface wave signals by performing preprocessing and/or postprocessing steps that are often ad hoc and may only work well for a specific dataset.

In the present paper, we develop a simple workflow, based on the idea of three-station interferometry proposed by Zhang et al. (2020), that effectively enhances surface waves, particularly at high frequencies, for ANCs of a 1-D linear array. We apply this method to data recorded by a dense linear array deployed at the Ramona Reservation (RR) site across surface traces of the San Jacinto fault, near Anza (Fig. 1). Seismic waveforms from the RR array have been analyzed for fault zone internal structures in Qin et al. (2020). ANCs were computed for each station pair of the RR array in Wang et al. (2019). To enhance surface waves with low SNR in ANCs at high frequencies, Wang et al. (2019) first applied a period-dependent tapering window and then applied double-beamforming tomography to derive Rayleigh wave phase velocities for periods from 0.3 s to 0.8 s beneath the array.

Here, we first describe station configuration and ANC data of the RR array in section 2. Then, in section 3, following the flow chart illustrated in Figure 2, we present the theoretical formulation for three-station interferometry using ANCs of a 1-D linear array and illustrate the surface wave denoising process with a subset of ANC data computed from the linear segment of the RR array. In section 4, surface wave phase travel times are

first extracted from the denoised wavefield and then inverted for phase velocity dispersion models via the eikonal equation. Discussion of the denoising method and comparison between the resulting phase velocity profiles and fault zone images from previous studies (Qin et al., 2020; Wang et al., 2019) are presented in section 5.

2. Data

The RR array (red triangle in Fig. 1b) is located at north of Anza (blue square in Fig. 1b), California, and crosses surface traces of the Clark segment of the San Jacinto fault (Fig. 1a). The array consists of 94 three-component 5-Hz Fairfield geophones (balloons in Fig. 1a) that were set to record continuously for a month with a sampling rate of 500 Hz. ANC is obtained by first computing cross correlations of ambient noise data in 5-min windows, and then stacking them over the entire recording period for each station pair (Wang et al., 2019). The positive and negative time lags of the monthlong stacked ANC are fold and averaged to suppress the effects of the asymmetric noise source distribution. We use ANCs of a sub-array RR01-RR47 (yellow, blue, and red balloons in Fig. 1a) to demonstrate the surface wave denoising process (Fig. 2a) developed in this study. The sub-array has 47 stations with an average station spacing of ~30 m and an aperture of ~1.6 km.

We project stations in the sub-array to the straight line connecting RR01 and RR47 (cyan dashed line in Fig. 1a) and compare interstation distances calculated using station locations before and after the projection. The comparison yields negligible differences (< 1%) suggesting that the sub-array RR01-RR47 is in a 1-D linear configuration (later referred to as “the linear RR array”). In Wang et al. (2019), a period-dependent velocity threshold is applied to taper off the contamination of body waves or potential higher-mode surface waves. In this study, however, we use a tapering window, between a moveout velocity range of 2 km/s and 0.1 km/s (white dashed lines in Figs. 1c-d), to ANCs of Transverse-Transverse (TT) and Vertical-Vertical (ZZ) components. The tapered ANCs are then filtered between 0.2 Hz and 10 Hz and depicted as colormaps in Figures 1c-d. Before performing surface wave denoising (Section 3) and tomography (Section 4) illustrated in Figure 2, a series of Gaussian narrow bandpass filters centered on consecutive periods between 0.3 s and 1.6 s are applied to the ANCs shown in Figures

1c-d and then each filtered waveform is normalized by its corresponding maximum. The Gaussian narrow bandpass filters are generated following section 3.1 of Qiu et al. (2019).

3. Surface Wave Denoising

Let $G_{i\_j}(t)$ be the positive lag of ANC for the station pair of i-th (virtual source) and j-th (virtual receiver) sensors in the linear RR array (yellow, green, and red triangles in Fig. 1a), we can expand it as

$$G_{i\_j}(t) = S_{i\_j}(t) + B_{i\_j}(t) + N_{i\_j}(t), \tag{1}$$

where $S_{i\_j}(t)$ and $B_{i\_j}(t)$ represent signals traveling on the surface (i.e. surface waves) and at depth (i.e. body waves) between the source i and receiver j, respectively. $N_{i\_j}(t)$ is the residual (later referred to as "background noise"). This section aims to develop a denoising process that preserves $S_{i\_j}(t)$ while suppressing $B_{i\_j}(t)$ and $N_{i\_j}(t)$ in equation 1.

3.1 Three-station interferometry for a 1-D linear Array

Since surface waves are dispersive, let $\tilde{G}_{i\_j}(\omega)$ be the Fourier transform of $G_{i\_j}(t)$ at the angular frequency ω, we can rewrite equation 1 in the frequency domain

$$\begin{aligned}\tilde{G}_{i\_j}(\omega) &= A_{G\_ij} \cdot e^{i\cdot\varphi_{G\_ij}} = \tilde{S}_{i\_j}(\omega) + \tilde{B}_{i\_j}(\omega) + \tilde{N}_{i\_j}(\omega) \\ &= \sum_{S} A_{S\_ij} \cdot e^{-i\left(\omega\cdot T_{ij}^{S}+\varphi_s\right)} + \sum_{B} A_{B\_ij} \cdot e^{-i\left(\omega\cdot T_{ij}^{B}+\varphi_B\right)} + \tilde{N}_{i\_j}(\omega),\end{aligned} \tag{2a}$$

where A_{S_ij} and T_{ij}^{S} are amplitude spectrum and phase travel time of surface wave signals in ANC at the angular frequency ω that propagate between the i-th and j-th stations, while A_{B_ij} and T_{ij}^{B} represent those of body wave signals. φ_s and φ_B are initial phases of surface- and body-wave signals in the ANC, respectively, and dependent on the distribution of ambient noise sources (e.g., Lin et al., 2008). Since the fundamental mode surface wave, $\tilde{F}_{i\_j}(\omega)$, is often the dominant signal in ANC, by assuming the higher-mode surface waves are negligible, we, therefore, can simplify equation 2a as:

$$\tilde{G}_{i\_j}(\omega) = \tilde{F}_{i\_j}(\omega) + \tilde{O}_{i\_j}(\omega) = A_{F\_ij} \cdot e^{-i\left(\omega\cdot T_{ij}^{F}+\varphi_F\right)} + \tilde{O}_{i\_j}(\omega), \tag{2b}$$

where the symbol or subscript F stands for the fundamental mode surface wave. $\tilde{O}_{i\_j}(\omega) = \tilde{B}_{i\_j}(\omega) + \tilde{N}_{i\_j}(\omega)$, that consists of signals from body waves and background noise, is the term we want to suppress in the denoising process. It is interesting to note

that $\varphi_F = \pi/4$ for an azimuthally homogenous ambient noise source distribution (Snieder, 2004), whereas $\varphi_F = 0$ when noise sources are only present in line with the station pair *i* and *j* (Lin et al., 2008).

For surface waves of a certain (e.g., fundamental) mode traveling between three stations $i < j < k$ in a 1-D linear array, the travel times satisfy the following relation

$$T_{ik}^S = T_{ij}^S + T_{jk}^S, \tag{3a}$$

whereas

$$T_{ik}^B < T_{ij}^B + T_{jk}^B, \tag{3b}$$

for body waves. Therefore, we introduce a third station *k* and perform three-station interferometry following Zhang et al. (2020):

$$\tilde{I}_{i\_j}(\omega; k) = \begin{cases} \tilde{G}_{i\_k}^*(\omega) \cdot \tilde{G}_{j\_k}(\omega), & k < i \\ \tilde{G}_{i\_k}(\omega) \cdot \tilde{G}_{j\_k}(\omega), & i < k < j. \\ \tilde{G}_{i\_k}(\omega) \cdot \tilde{G}_{j\_k}^*(\omega), & k > j \end{cases} \tag{4a}$$

In equation 4a, we cross correlate $G_{i\_k}(t)$ and $G_{j\_k}(t)$ in the time domain, when $k < i$ or $k > j$ (later referred to as "outer-source zone"). The interferometry becomes equivalent to the convolution of $G_{i\_k}(t)$ and $G_{j\_k}(t)$ in the time domain for station *k* located within the two virtual sources (i.e., $i < k < j$; later referred to as "inter-source zone"). For the case $k = i$ or *j*, we define $\tilde{I}_{i\_j}(\omega; k) = A_{G\_ij}^2 \cdot e^{i \cdot \varphi_{G\_ij}}$ that approximates the convolution of $G_{i\_j}(t)$ and $G_{i\_i}(t)$ or $G_{j\_j}(t)$, by assuming the amplitude spectrum of the auto-correlation $G_{i\_i}(t)$ or $G_{j\_j}(t)$ is similar to that of $G_{i\_j}(t)$, i.e., $A_{G\_ii} \approx A_{G\_jj} \approx A_{G\_ij}$.

Combining equations 2b, 3a, and 4a, if the fundamental mode surface wave is the dominate signal in ANC (i.e., $\tilde{O}_{i\_j}$ in Equation 2b is negligible), phase term of the interferogram $\tilde{I}_{i\_j}(\omega; k) = A_{ij\_k} \cdot e^{i \cdot \varphi_{ij\_k}}$ is given by

$$\varphi_{ij\_k}(\omega) = \begin{cases} -\omega \cdot T_{ij}^F - 2\varphi_F, & i < k < j \\ -\omega \cdot T_{ij}^F - \varphi_F, & k = i \; or \; j. \\ -\omega \cdot T_{ij}^F, & k > i \; or \; k < j \end{cases} \tag{4b}$$

φ_F and T_{ij}^F denote the initial phase and phase travel time of the fundamental mode surface wave signal (Equation 2b) extracted from the ANC of station pair *i* and *j*. Equation 4b suggests that the interferograms within either the inter- or outer-source zones share the same phase, whereas interferograms from different zones are only aligned in phase when

φ_F is zero. In cases when the term $\tilde{O}_{i\_j}$ is significant, we can divide the interferogram $\tilde{I}_{i\_j}(\omega;k)$ into two components: $\tilde{I}^F_{i\_j}(\omega;k)$ and $\tilde{I}^O_{i\_j}(\omega;k)$. $\tilde{I}^F_{i\_j}(\omega;k)$ represents the interferogram that only involves the fundamental mode surface wave signal, i.e., when $\tilde{O}_{i\_j}$ is set to zero. The phase of $\tilde{I}^F_{i\_j}(\omega;k)$, given by equation 4b, is independent of k when φ_F is zero. In contrast, $\tilde{I}^O_{i\_j}(\omega;k)$ engages contributions from body waves and background noise, and thus has a phase that varies significantly with k.

3.2 Surface wave denoising of the linear RR Array

As described in section 2, we first apply a series of Gaussian narrow bandpass filters centered on periods between 0.3 s and 1.6 s to the ANCs of the linear RR array (Figs. 1c-d). The period range is determined based on the station spacing and array aperture. Then the denoising process (Fig. 2a) is performed on the filtered ANCs for each period and component separately. Figure 3 shows results of the three-station interferometry applied to ANCs of TT component filtered at 0.3 s (Figs. S1a-c for 0.8 s and Figs. S2a-c & S3a-c for ZZ component) for an example station pair RR10 (i = 10) and RR40 (j = 40). The ANCs with RR10 and RR40 as the virtual source, $G_{i\_k}(t)$ and $G_{j\_k}(t)$ filtered at 0.3 s, are shown in Figures 3a and 3b, respectively. Black and blue waveforms denote ANCs with station k inside the outer-source (k < 10 or k > 40) and inter-source (10 < k < 40) zones, respectively, whereas the ANC of station pair RR10 and RR40 is depicted in red (i.e., k is the y-axis of Fig. 3).

Figure 3c demonstrates the resulting interferograms in the time domain computed following equation 4a (blue for convolution, black for cross correlation). Both the phase and envelope functions of the interferograms vary significantly with station k. Such k-value-dependent interferograms are also observed using ZZ component ANCs filtered at 0.3 s (e.g., Fig. S2c). This is because of the low SNR for the fundamental mode surface wave (i.e., $\tilde{O}_{i\_j}$ in Equation 2b is non-negligible) in the ANCs filtered at 0.3 s (e.g., Figs. 3a-b and S2a-b). On the other hand, the interferograms are coherent and aligned well in phase for all k values at 0.8 s (e.g., Figs. S1c and S3c), when high-quality signals of the fundamental mode surface wave are observed in the filtered ANCs (e.g., Figs. S1a-b and S3a-b). This suggests that the initial phase φ_F is zero, i.e., $\varphi_{ij\_k}(\omega) = -\omega \cdot T^F_{ij}$ (Equation 4b), for ANCs of the linear RR array filtered at 0.8 s. We also verified that the initial

phase φ_F is zero for all periods (from 0.3 s to 1.6 s) analyzed in this study, by estimating the systematic phase difference between interferograms in the inter- and outer-source zones computed for the example station pair RR10 and RR40 (not shown here).

Therefore, we can simply stack the interferograms $\tilde{I}_{i\_j}(\omega;k) = A_{ij\_k} \cdot e^{i\cdot\varphi_{ij\_k}}$, defined in equation 4a, over all available station k to enhance the contribution from the fundamental mode surface wave, $\tilde{I}^F_{i\_j}(\omega;k)$, which has a phase that is independent of k (Equation 4b with $\varphi_F = 0$). The other component, $\tilde{I}^O_{i\_j}(\omega;k)$, that involves contributions from body waves and background noise is suppressed through stacking, as its phase varies significantly with k (Section 3.1). The denoised waveform obtained through linear stacking is given by:

$$\tilde{C}^3_{i\_j}(\omega) = \sum_{k=1}^{N} e^{i\cdot\varphi_{ij\_k}} \sqrt{A_{ij\_k}} \Big/ N. \tag{5a}$$

Here, N is the number of stations in the 1-D linear array. We take the square root of the amplitude spectrum A_{ij_k} in Equation 5a to suppress the effect of source spectra multiplication introduced in the three-station interferometry (Equation 4a). This is based on the assumption that amplitude spectra of the filtered ANCs are similar for all station pairs, i.e., $A_{ij\_k} = A_{G\_ik} \cdot A_{G\_jk} \approx \hat{A}^2_G$.

In this study, we perform phase weighted stacking rather than linear stacking, as phase weighted stacking is more efficient in suppressing incoherent patterns and has negligible effects on phase measurements (e.g., Fig. S4; Schimmel and Paulssen, 1997). Let $\hat{C}^3_{i\_j}(t;\omega_c)$ be the waveform in time domain denoised through linear stacking using ANCs filtered at the angular frequency ω_c, the corresponding waveform denoised through phase weighted stacking in the time domain is given by

$$C^3_{i\_j}(t;\omega_c) = W_{i\_j}(t;\omega_c) \cdot \hat{C}^3_{i\_j}(t;\omega_c), \tag{5b}$$

where $W_{i\_j}(t;\omega_c)$ is a weighting function that indicates the phase coherence of interferograms in the time domain (e.g., Fig. 3c) averaged over all k values.

3.3 Results

Figure 4a shows the comparison between the TT component ANC (black) of the example station pair RR10 and RR40 filtered at 0.3 s and the corresponding denoised

waveforms, computed through linear stacking (blue; Equation 5a) and phase weighted stacking (bottom red curve; Equation 5b). Although coda waves in the denoised waveform $C_{i\_j}^{3}(t;\omega_c)$ are greatly suppressed, the fundamental mode surface wave is still not the dominant signal (e.g., large-amplitude wavelets before the surface wave). This is likely due to the poor SNR of surface waves in the ANCs filtered at 0.3 s (Figs. 3a-b). Therefore, we further enhance the surface wave signal by repeating the denoising process (Fig. 2a): first self-normalize the output wavefield of the current iteration, and then use the normalized wavefield as the input for the next iteration. The number of iterations is determined so that the difference between input and output wavefields of the last iteration is negligible (Fig. 2a).

We use symbol $C_{i\_j}^{2+n}(t;\omega_c)$ to represent the waveform of station pair i and j, after applying n (≥ 1) iterations of the denoising process described in section 3.2 to ANCs filtered at angular frequency ω_c. Figure 4a suggests that four more iterations (red waveforms; n = 5) are needed to obtain surface waves with sufficient quality from the ANCs filtered at 0.3 s, i.e., the difference between the input, $C_{i\_j}^{6}(t;\omega_c)$, and output, $C_{i\_j}^{7}(t;\omega_c)$, waveforms is visually negligible. Although the SNR gradually increases in waveforms from bottom to top (Fig. 4a), the surface wave signal is always coherent and aligned in phase. As the SNR is much higher for surface waves in ANCs filtered at low frequencies (> 0.6 s), the number of iterations used to extract good quality surface waves is smaller (n = 3; e.g., 0.8 s in Fig. S1d).

Comparison between the TT component ANC data $G_{i\_j}(t;\omega_c)$ filtered at 0.3 s and the denoised waveforms $C_{i\_j}^{7}(t;\omega_c)$ is illustrated in Figures 4b-c for all station pairs. Although coherent fundamental mode surface waves are seen propagating at a group velocity slightly slower than 0.5 km/s in the filtered ANC data (Fig. 4b), wavelets with large amplitudes are observed before and after the surface wave signals (e.g., black waveform in Fig. 4b). The large amplitude waves arriving prior to the surface wave are likely related to the tapering window at short interstation distances (e.g., < 1 km), as the apparent moveout velocity is 2 km/s (the upper limit velocity of our tapering window; Section 2). At long interstation distances, the precursor wavelets have an apparent moveout velocity of ~1 km/s and may represent the contribution from body wave energy.

These waves that we want to suppress in the denoising process are sometimes even larger than the surface wave signal in the filtered ANCs (e.g., black waveform in Fig. 4b).

After five iterations of the denoising process for ANCs filtered at 0.3 s, surface wave signals are well preserved whereas the other signals are greatly suppressed (Fig. 4c). The amplitude spectra averaged over all station pairs for data before (in black) and after (in red) denoising are demonstrated in Figure 4d. The observation of a smoother mean amplitude spectrum after denoising (red curve in Fig. 4d) suggests that the difference between amplitude spectra of every two station pairs is much smaller. Since SNR of the fundamental mode surface wave is much larger in ANCs filtered at 0.8 s (Figs. S1a-b and S3a-b), the difference between waveforms before and after denoising is still noticeable but much smaller (Figs. S1e-g and S3e-g). As the fundamental mode surface wave is the dominant signal after denoising (e.g., Figs. 4c and S1f-S3f), all results in section 4 refer to the fundamental mode surface wave.

4. Surface Wave Tomography

In this section, we use waveforms of TT and ZZ components denoised at each period (e.g., Figs. 4c and S1f-S3f) to infer phase velocity structures of Love and Rayleigh waves beneath the array, respectively. Following the flow chart shown in Fig. 2b, we first determine cycle-skipped phase travel times of surface waves propagating between all available station pairs at each period (e.g., Fig. 5a) in the frequency domain, which is much simpler than measuring in the time domain but requires high SNR (Section 4.1). Second, we infer phase velocity structures beneath the linear RR array, using travel time measurements after cycle-skipping correction from section 4.1, via the eikonal equation in section 4.2 (e.g., Fig. 5b). The aim of this section is to demonstrate that robust surface wave phase velocity models can be resolved from the denoised waveforms.

4.1 Determination of phase travel time

Frequency time analysis (FTA) is widely used in previous studies to determine phase travel time of surface wave in ANC (e.g., Bensen et al., 2007; Lin et al., 2008; Qiu et al., 2019). First, Gaussian narrow bandpass filters centered on a series of consecutive frequencies are applied to the ANC, then the phase travel time dispersion is measured using the envelope and phase functions of the filtered ANC in the time domain. The

advantage of FTA is that reliable phase travel times can still be extracted when SNR is low at high frequencies. However, ad hoc criteria and thresholds are required to automate the FTA. Additional details on the FTA method can be found in section 3 of Qiu et al. (2019). Since our goal is to verify that the signals after denoising are representative of surface waves and high SNR is achieved for all frequencies, we thus measure phase travel times from the denoised waveforms in the frequency domain, which is much simpler than the FTA method.

Although surface wave is the dominant signal in the denoised waveform, we still observe waves with small amplitudes before and after the surface wave (e.g., black waveform in Fig. 4c). This is because we can only suppress rather than remove signals that are not surface waves. Here, we apply a tapering window (e.g., black dashed lines in Figs. S5d-S8d) centered on the surface wave to further remove these background signals. Width of the tapering window is set to four times the dominant period of the array-mean amplitude spectrum (e.g., red curve in Fig. 4d), whereas the center is determined by the average phase and group velocities of the array (e.g., red and cyan stars in Figs. S5b). Details of the tapering window can be found in Text S1.

Assuming these background signals are negligible after denoising and tapering (e.g., blue waveform in Fig. 5a), combining equation 2b and $\varphi_F = 0$, we have

$$\tilde{C}_{i\_j}^{DT}(\omega;\omega_c) = A_{F\_ij}(\omega;\omega_c)e^{-i\cdot\omega T_{ij}^{F}(\omega)}, \tag{6}$$

where $\tilde{C}_{i\_j}^{DT}(\omega;\omega_c)$ is the spectrum of the tapered waveform that is denoised at the angular frequency ω_c for station pair i and j. Equation 6 suggests that we can extract cycle-skipped phase travel time from the phase spectrum of the tapered waveform. Therefore, we measure the wrapped phase (i.e., between -2π and 0) of the spectrum $\tilde{C}_{i\_j}^{DT}(\omega;\omega_c)$ at the peak frequency $f_{\max}$ (3.2 Hz; e.g., dashed line in Fig. 4d) of the array-mean amplitude spectrum, where the array-mean SNR of the surface wave is the highest. Then, the cycle-skipped phase travel time is computed as the wrapped phase divided by $-2\pi f_{\max}$.

Figure 5a shows the cycle-skipped phase travel time (white circles) measured for surface waves filtered at 0.3 s from station pairs associated with a common virtual source RR10 (y-axis of 0 km). To obtain the actual phase travel time, we perform a simple cycle-skipping correction as follows:

(1) Similar to Figure 5a, we first extract all the cycle-skipped phase travel times for surface waves of a virtual shot gather and arrange them as a function of the location to the virtual source.
(2) We perform cycle-skipping correction for surface waves traveling NE (toward RR47) and SW (toward RR01) separately.
(3) For surface waves traveling in the same direction, the principle of the cycle-skipping correction is to ensure that the travel time of any virtual receiver is larger than those of receivers that are closer to the virtual source after the correction.
(4) In practice, we examine measurements T_i and T_{i+1} of every two adjacent virtual receivers with the i-th station being closer to the virtual source. If $T_i \geq T_{i+1}$, we use T_i as the reference and add $N/f_{\max}$ (N is an integer) to T_{i+1} so that $T_{i+1}+N/f_{\max} > T_i \geq T_{i+1}+(N\text{-}1)/f_{\max}$. The correction is performed for closer-to-source pairs first.

Travel times, for the virtual shot gather of RR10, after the correction are illustrated as red stars in Figure 5a. We note that a more sophisticated cycle-skipping correction (e.g., using phase velocity structure inferred at a longer period as the reference) is needed when station spacing is larger than one wavelength.

4.2 1-D eikonal tomography

We use the eikonal equation to derive phase velocity structures using travel time measurements of all station pairs in the linear RR array (Section 4.1). First, we project all stations to the straight line connecting RR01 and RR47 (cyan dashed line in Fig. 1a). Second, travel time measurements associated with each virtual source i at the target frequency $f_{\max}$ are extracted and interpolated (e.g., black curve in Fig. 5a) with a regular grid size of Δ=50 m. Since variations in topography (Fig. 2b of Qin et al., 2020) have a negligible effect (< 0.5%) on the results, the eikonal tomography can be simplified as:

$$\tilde{v}_i(x; f_{\max}) = 2 \cdot \Delta / [T_i(x + \Delta; f_{\max}) - T_i(x - \Delta; f_{\max})], \quad (7)$$

where $\tilde{v}_i(x; f_{\max})$ and $T_i(x; f_{\max})$ are the local phase velocity and interpolated phase travel time, respectively, of the grid cell at location x. Since the local phase velocity $\tilde{v}_i$ only varies with the grid cell location, it is independent of virtual source i. Thus, we can average the 1-D phase velocity profiles resolved from all available virtual sources at the same frequency $f_{\max}$ to achieve a more reliable phase velocity model:

$$\bar{v}(x; f_{\max}) = \sum_{i=1}^{N_x} \tilde{v}_i(x; f_{\max}) \Big/ N_x, \tag{8a}$$

and estimate the corresponding uncertainty as the standard deviation:

$$\delta(x; f_{\max}) = \sqrt{\sum_{i=1}^{N_x} [\tilde{v}_i(x; f_{\max}) - \bar{v}(x; f_{\max})]^2 \Big/ N_x}, \tag{8b}$$

where N_x is the number of virtual sources available for stacking at location x.

In surface wave studies, phase velocities derived at near-virtual-source grid cells are often excluded to satisfy the far-field approximation (e.g., Bensen et al., 2007). The size of the exclusion zone is usually multiples of the analyzed wavelength (e.g., one wavelength in Wang et al., 2019). Here, however, we set an exclusion zone with a fixed size of 100 m, i.e., discard phase velocities derived at the four grid cells closest to the virtual source. Figure 5b shows the 1-D phase velocity profile, in white dots, derived using measurements associated with the virtual source RR10 (black curve in Fig. 5a) for Love waves at 3.2 Hz (~0.3 s), whereas phase velocity profiles resolved from all virtual sources are illustrated in gray curves and as the colormap. The average phase velocity and uncertainty profiles are calculated via equation 8 and demonstrated as red stars and error bars, respectively, in Figure 5b. Results for Love waves at a lower frequency (~0.8 s) and those of Rayleigh waves are shown in Figures S9 and S10-S11, respectively.

Figure 6 shows phase velocity models resolved at periods ranging from 0.3 s to 1.6 s for Love waves (Fig. 6a) and 0.3 s to 1.3 s for Rayleigh waves (Fig. 6b), together with the corresponding uncertainty estimations (Figs. 6c-d). The period range in the plot is determined so that the resolved maximum uncertainty is smaller than 0.1 km/s. In general, the uncertainties are smaller than 0.03 km/s for both Rayleigh and Love waves at all analyzed periods, indicating the resolved phase velocity structures are robust and reliable. This also justifies our choice of an exclusion zone with a 100-m-radius, as one wavelength at low frequency (e.g., ~900 m for Rayleigh wave at ~0.8 s; Fig. S11b) is much larger than 100 m. We note that results of Love waves at ~0.4 s are excluded here due to anomalous large uncertainties (Fig. S12b). This is due to the observation of non-negligible signals, likely representing higher-mode surface waves, traveling at a different phase speed compared to that of the fundamental mode Love waves (Figs. S13-S14). We

note that reliable phase travel times can still be measured for the fundamental mode Love waves at ~0.4 s if FTA is used.

Phase velocity models of both Love and Rayleigh waves show a ~500- to 1000-m-wide low-velocity zone at low frequencies (e.g., > 0.8 s) that gradually narrows with the period. Combined with the fact that phase velocity at lower frequency is more sensitive to structures at greater depth, this observation likely indicates a flower-shaped (i.e., width decreases with depth) fault damage zone beneath the linear RR array. We also see several ~100-m-wide narrow zones, that are close to the mapped fault surface traces (black dashed lines in Figs. 6a-b), with extremely low phase velocities (< 500 m/s) at high frequencies (e.g., 0.3-0.6 s). However, the shape and location of these low-velocity zones are different between Figures 6a and 6b. In addition, complicated patterns of low-velocity anomalies at various scales in both phase velocity models (Figs. 6a and 6b) suggest high degrees of heterogeneity in shear wave velocity structures beneath the linear RR array. Structure patterns that are inconsistent between models of Love and Rayleigh waves may indicate the existence of radial anisotropy or complicated structures of Vp/Vs ratio.

5. Discussion

We compare the Rayleigh wave phase velocity models derived from this study and Wang et al. (2019) in the overlapping period (0.3-0.8 s) and spatial (RR01-RR47) ranges (Fig. 7). The same ANC dataset of ZZ component is utilized in Wang et al. (2019) to derive the phase velocity model (Fig. 7b) for Rayleigh waves. In their study, double beamforming technique is used, where the local phase velocity is obtained through grid search: first sum all ANCs of two sub-arrays (three nearby stations) via slant-stacking with different velocity values, then determine the local phase velocity of each sub-array based on the maximum amplitude of the envelope function for the stacked waveform. Through slant-stacking, Wang et al. (2019) was able to enhance the low SNR surface waves in ANCs at high frequencies and generate a robust phase velocity model.

In general, consistent velocity values and structural patterns are observed in both phase velocity models, such as an ultra-low velocity (< 0.4 km/s) zone on the NE side of the middle fault surface trace (F2 in Figs. 7a-b). This indicates that the enhanced signals in ANCs after denoising are surface waves. It is also important to note that our Rayleigh

384 wave phase velocity model covers a wider period range (0.3-1.3 s; Fig. 6b) compared to
385 that of Wang et al. (2019) (0.3-0.8 s). There are two reasons for that: first, we only
386 exclude data associated with station pairs that are less than 100 m apart, whereas the size
387 of exclusion zone is one wavelength in Wang et al. (2019); second, phase velocities
388 inferred from slant-stacking have much larger uncertainties than those derived from
389 travel times, as the peak of envelope function is much sensitive to noise than phase
390 function (e.g., Section 3.3 of Qiu et al., 2019), at longer periods.

391 The uncertainties estimated from this study (Fig. 7c) are significantly smaller than
392 those of Wang et al. (2019) (Fig. 7d), suggesting the phase velocity structure is better
393 constrained in this study, particularly near the fault surface traces (e.g., NE of F3 and
394 between F1 and F2 in Fig. 7) and at high frequencies (e.g., < 0.6s). The larger uncertainty
395 values observed in Wang et al. (2019) are likely due to the low SNR of surface waves in
396 ANCs at high frequencies and should be significantly reduced if the denoised waveforms
397 (e.g., Fig. 4c) are used. By comparing phase velocity models resolved from this study and
398 Wang et al. (2019), we demonstrate that fundamental mode surface waves in ANCs are
399 successfully enhanced through the proposed denoising method. Besides, phase velocity
400 structures are better constrained (i.e., much smaller uncertainties) using the denoised
401 waveforms in this study than those inferred from the raw ANCs in Wang et al. (2019).

402 The derivations presented in section 3.1 are based on two assumptions: higher-mode
403 surface waves are negligible, and stations are aligned in a straight line. After performing
404 the denoising process on ANCs of the linear RR array filtered at different periods
405 between 0.3 s and 1.6 s for TT and ZZ components, we do not observe higher-mode
406 surface waves except for TT component data filtered at 0.4 s (Figs. S13-S14). Even when
407 higher-mode surface waves are present, we further demonstrate that the denoising process
408 based on three-station interferometry will only enhance surface waves of each mode
409 separately in Text S2. Regarding the effect of array geometry, we do not investigate in
410 detail the bias in surface wave travel times measured from the denoised waveforms when
411 stations are not perfectly aligned in a straight line. Assuming the velocity structure is
412 homogenous perpendicular to the strike direction of the array, the station-configuration
413 error is proportional to the difference between interstation distances calculated using
414 station locations before and after projecting the array to a straight line (e.g., Fig. 1a).

For a rough estimation, the mean and maximum differences between interstation distances of the linear RR array calculated before and after the linear projection (Section 2) are ~0.1% and 1%, respectively. The uncertainties estimated from eikonal tomography (Figs. 6c-d) suggest ~0.5-1% and ~3% for the mean and maximum perturbations in the resolved phase velocities, which is comparable and larger than the bias in array geometry. Therefore, we conclude that this denoising method is still robust when the station-configuration error is less than the allowable uncertainty of the resulting phase velocity model (e.g., mean and maximum of 1% and 3% in this study). Surface wave denoising of ANCs computed from arrays in a 2-D configuration (e.g., include all stations in the RR array) will be the subject of a future study.

Although we only illustrate the denoising method using ANCs computed following the preprocessing steps described in Wang et al. (2019), it can be applied to any noisy wavefield that consists of surface waves propagating within a linear array. Therefore, this method can be used as a routine postprocessing procedure for improving the quality of surface waves in ANCs of a linear array with any type of preprocessing steps (e.g., coda wave C^3 or C^N; Froment et al., 2011). After denoising, we may be able to perform surface wave studies on data from linear array deployments that were previously considered to be too short in recording duration or too "noisy" (i.e., deployed during high seismic activity period) to retrieve good quality surface wave signals from ANCs.

We note that Lin et al. (2009) used the term "apparent phase velocity" for the phase velocity resolved from the eikonal equation (Equation 8a). They concluded that the apparent phase velocity is accurate when the wave frequency is sufficiently high or the wave amplitude is varying smoothly in space. Otherwise, a correction term must be added (Lin & Ritzwoller, 2011). Considering the linear RR array is dense (average station spacing of ~30 m) and deployed crossing fault damage zones that can significantly amplify seismic motions (Qin et al., 2020), both the "high frequency" and "smooth amplitude variation" approximations are likely violated for phase velocity models derived in section 4.2. Therefore, we propose performing travel-time based full waveform tomography (e.g., Zhang et al., 2018) on the denoised surface waves, rather than inverting the "apparent" phase velocity models (Figs. 6a-b), to infer shear wave velocity structures beneath the linear RR array as the subject of a future study.

In the present study, we only show the denoised ANCs filtered at frequencies up to ~3 Hz (Figs. 4 and S2d-g) by requiring a minimum wavelength of 150 m (i.e., the maximum station spacing) for eikonal tomography (Section 4). However, this denoising method can be applied to ANCs at even higher frequencies when surface wave signals are present (e.g., ~5 Hz in Figs. S15-S16). Using high-quality surface waves denoised from ANCs of linear arrays crossing major fault zones for a wide range of frequencies (e.g., 0.5-5 Hz in this study; 2-40 Hz in Zigone et al., 2019), shear wave velocity model that extends to both shallow (top few tens of meters) and deep (top few kilometers) structures can be derived. Such fault zone velocity model with unprecedented high-resolution will complement the qualitative model inferred from traditional fault zone analyses (e.g., Qin et al., 2018, 2020; Qiu et al., 2017, 2020; Share et al., 2017, 2019). An integration of both quantitative and qualitative fault zone models can have significant implications for seismic hazard evaluations (e.g., Ben-Zion & Shi, 2005; Spudich & Olsen, 2001) and long-term behavior of the fault (e.g., Thakur et al., 2020).

6. Conclusions

We demonstrate the effectiveness and robustness of the three-station-interferometry-based surface wave denoising method using ANCs of the linear RR array, particularly at high frequencies (e.g., > 2 Hz). The proposed surface wave denoising method can be applied to a wide range of topics in the future using data recorded by 1-D linear arrays:

1. Reduce the minimum duration of ambient noise recording and preprocessing steps needed to achieve high-quality surface waves from ANCs.
2. Obtain good quality surface waves from ANCs computed for fault zone linear arrays deployed right after a major earthquake (e.g., fault zone arrays in Ridgecrest area; Catchings et al., 2020) without applying any sophisticated preprocessing steps.
3. Provide high-quality surface wave signals both at high (> 2 Hz) and low frequencies (< 1 Hz) for better constraints of shallow (top 10s to 100s of meters) materials through full-waveform surface wave tomography.
4. Investigate the initial phase φ_F (Equation 2b) for a wider frequency band and arrays at different locations, and its relation to the ambient noise source distribution

Acknowledgements

We thank Fan-Chi Lin and Elizabeth Berg for providing the ambient noise cross correlation data and Rayleigh wave phase velocity model of Wang et al. (2019), and Nori Nakata and Benxin Chi for useful discussions. Continuous seismic recordings of the RR array are available through the International Federation of Digital Seismography Networks (Allam, 2015; https://www.fdsn.org/networks/detail/9K_2015/). This work was supported by Rice University and the National Science Foundation (Award EAR-1251667).

References

Allam, A.A. (2015), San Jacinto damage zone imaging arrays. International Federation of Digital Seismograph Networks. Dataset/Seismic Network. Doi: https://doi.org/10.7914/SN/9K_2015

Ben-Zion, Y., & Shi, Z. (2005). Dynamic rupture on a material interface with spontaneous generation of plastic strain in the bulk. *Earth and Planetary Science Letters*. https://doi.org/10.1016/j.epsl.2005.03.025

Bensen, G. D., Ritzwoller, M. H., Barmin, M. P., Levshin, A. L., Lin, F.-C., Moschetti, M. P., et al. (2007). Processing seismic ambient noise data to obtain reliable broad-band surface wave dispersion measurements. Geophysical Journal International, 169(3), 1239–1260. https://doi.org/10.1111/j.1365-246X.2007.03374.x

Catchings, R. D., Goldman, M. R., Steidl, J. H., Chan, J. H., Allam, A. A., Criley, C. J., et al. (2020). Nodal Seismograph Recordings of the 2019 Ridgecrest Earthquake Sequence. *Seismological Research Letters*. https://doi.org/10.1785/0220200203

Curtis, A., Nicolson, H., Halliday, D., Trampert, J., & Baptie, B. (2009). Virtual seismometers in the subsurface of the Earth from seismic interferometry. Nature Geoscience. https://doi.org/10.1038/ngeo615

Froment, B., Campillo, M., & Roux, P. (2011). Reconstructing the Green's function through iteration of correlations. Comptes Rendus - Geoscience. https://doi.org/10.1016/j.crte.2011.03.001

Lin, F.-C., & Ritzwoller, M. H. (2011). Apparent anisotropy in inhomogeneous isotropic media. *Geophysical Journal International*. https://doi.org/10.1111/j.1365-246X.2011.05100.x

Lin, F.-C., Moschetti, M. P., & Ritzwoller, M. H. (2008). Surface wave tomography of the western United States from ambient seismic noise: Rayleigh and Love wave phase velocity maps. Geophysical Journal International. https://doi.org/10.1111/j.1365-246X.2008.03720.x

Lin, F.-C., Ritzwoller, M. H., & Snieder, R. (2009). Eikonal tomography: Surface wave tomography by phase front tracking across a regional broad-band seismic array. Geophysical Journal International. https://doi.org/10.1111/j.1365-246X.2009.04105.x

Qin, L., Ben-Zion, Y., Qiu, H., Share, P. E., Ross, Z. E., & Vernon, F. L. (2018). Internal structure of the san jacinto fault zone in the trifurcation area southeast of anza, california, from data of dense seismic arrays. *Geophysical Journal International*, *213*(1), 98–114. https://doi.org/10.1093/gji/ggx540

Qin, L., Share, P.-E., Qiu, H., Allam, A. A., Vernon, F. L., & Ben-Zion, Y. (2020). Internal structure of the San Jacinto fault zone at the Ramona Reservation, north of Anza, California, from dense array seismic data. Geophysical Journal International. https://doi.org/10.1093/gji/ggaa482

Qiu, H., Ben-Zion, Y., Ross, Z. E., Share, P. E., & Vernon, F. L. (2017). Internal structure of the San Jacinto fault zone at Jackass Flat from data recorded by a dense linear array. *Geophysical Journal International*, *209*(3), 1369–1388. https://doi.org/10.1093/gji/ggx096

Qiu, H., Lin, F.-C., & Ben-Zion, Y. (2019). Eikonal tomography of the Southern California plate boundary region. Journal of Geophysical Research: Solid Earth, 2019JB017806. https://doi.org/10.1029/2019JB017806

Qiu, H., Ben-Zion, Y., Catchings, R., Goldman, M., Allam, A., & Steidl, J. (2020). Detailed seismic imaging of the Mw 7.1 Ridgecrest earthquake rupture zone from data recorded by dense linear arrays. https://doi.org/10.1002/essoar.10504611.1

Schimmel, M., & Paulssen, H. (1997). Noise reduction and detection of weak, coherent signals through phase-weighted stacks. Geophysical Journal International.

https://doi.org/10.1111/j.1365-246X.1997.tb05664.x

Share, P. E., Ben-Zion, Y., Ross, Z. E., Qiu, H., & Vernon, F. L. (2017). Internal structure of the San Jacinto fault zone at Blackburn Saddle from seismic data of a linear array. *Geophysical Journal International*, *210*(2), 819–832. https://doi.org/10.1093/gji/ggx191

Share, P. E., Allam, A. A., Ben-Zion, Y., Lin, F.-C., & Vernon, F. L. (2019). Structural Properties of the San Jacinto Fault Zone at Blackburn Saddle from Seismic Data of a Dense Linear Array. *Pure and Applied Geophysics*, *176*(3), 1169–1191. https://doi.org/10.1007/s00024-018-1988-5

Snieder, R. (2004). Extracting the Green's function from the correlation of coda waves: A derivation based on stationary phase. Physical Review E - Statistical Physics, Plasmas, Fluids, and Related Interdisciplinary Topics. https://doi.org/10.1103/PhysRevE.69.046610

Spudich, P., & Olsen, K. B. (2001). Fault zone amplified waves as a possible seismic hazard along the Calaveras fault in central California. *Geophysical Research Letters*. https://doi.org/10.1029/2000GL011902

Thakur, P., Huang, Y., & Kaneko, Y. (2020). Effects of Low-Velocity Fault Damage Zones on Long-Term Earthquake Behaviors on Mature Strike-Slip Faults. *Journal of Geophysical Research: Solid Earth*. https://doi.org/10.1029/2020JB019587

Wang, Y., Allam, A. A., & Lin, F.-C. (2019). Imaging the Fault Damage Zone of the San Jacinto Fault Near Anza With Ambient Noise Tomography Using a Dense Nodal Array. Geophysical Research Letters. https://doi.org/10.1029/2019GL084835

Zhang, C., Yao, H., Liu, Q., Zhang, P., Yuan, Y. O., Feng, J., & Fang, L. (2018). Linear Array Ambient Noise Adjoint Tomography Reveals Intense Crust-Mantle Interactions in North China Craton. *Journal of Geophysical Research: Solid Earth*. https://doi.org/10.1002/2017JB015019

Zhang, S., Feng, L., & Ritzwoller, M. H. (2020). Three-station interferometry and tomography: coda versus direct waves. Geophysical Journal International. https://doi.org/10.1093/gji/ggaa046

Zigone, D., Ben-Zion, Y., Lehujeur, M., Campillo, M., Hillers, G., & Vernon, F. L. (2019). Imaging subsurface structures in the San Jacinto fault zone with high-

frequency noise recorded by dense linear arrays. *Geophysical Journal International*, *217*(2), 879–893. https://doi.org/10.1093/gji/ggz069

Figure captions

Figure 1. (a) Google map for the RR array (colored balloons) deployment that crosses surface traces of the San Jacinto fault (colored lines). The stations colored in white are not analyzed in this study, whereas the green balloons denote three sensors closest to each corresponding fault surface trace. Surface wave denoising procedure is demonstrated for an example station pair (red balloons). (b) Zoom out map of the San Jacinto fault zone. The background colors indicate topography. The red star and blue square denote locations of the RR array and the town of Anza. The black lines illustrate surface traces of major faults in this area. EF – Elsinore Fault; SAF – San Andreas Fault; SJF – San Jacinto Fault. (c) Ambient noise cross correlations at TT component of all station pairs for the sub-array RR01-RR47. The cross correlations are arranged according to interstation distance with red and blue colors representing positive and negative values. All the waveforms are first tapered using a velocity range of 2 km/s and 0.1 km/s (dashed lines), and then bandpass filtered between 0.2 and 10 Hz. (d) Same as (c) for the ZZ component.

Figure 2. (a) Flow chart of the surface wave denoising and imaging procedure developed in this study. The dashed box outlines the part of the diagram that performs surface wave tomography. The workflow adopted in this study for surface wave tomography is shown in (b). ANC – Ambient Noise Cross-correlation.

Figure 3. (a) Ambient noise cross correlations (ANCs) of TT component narrow bandpass filtered at 0.3 s associated with the virtual source RR10 (red star). Waveforms are arranged by the station number of the virtual receiver. (b) Same as (a) for virtual source RR40. Waveforms in black and blue represent ANCs of virtual receivers in the outer- and inter-source zones, respectively, while the red waveform denotes the ANCs of the station pair of the two virtual sources RR10 and RR40 (red balloons in Fig. 1a). (c) Interferograms calculated via three-station interferometry (Equation 4a).

Figure 4. (a) Comparison between the ANC (red waveforms in Figs. 3a-b), linear stacked (LS) C3 (Equation 5a), and phase weighted stacked (PWS) C3 – C7 (Equation 5b) of the example station pair RR10 and RR40 at TT component. (b) ANCs of TT component (Fig. 1c) narrow bandpass filtered at 0.3 s with red and blue colors representing positive and negative values. The three white dashed lines illustrate moveout velocities of 2 km/s, 0.5 km/s, and 0.1 km/s. The black waveform denotes ANC of the example pair RR10 and RR40, i.e. bottom black waveform in (a). (c) PWS C7 of all station pairs at 0.3 s. The white dashed line denotes a moveout velocity of 0.5 km/s. The black waveform denotes PWS C7 of the example station pair RR10 and RR40, i.e. top red waveform in (a). (d) Array-mean amplitude spectra of waveforms (b) before and (c) after denoising are depicted in black and red, respectively. The peak frequency of the red amplitude spectrum is illustrated by the red dashed line and labeled in the top right of the panel (c).

Figure 5. (a) Love waves associated with the virtual source RR10 after denoising at 0.3 s and tapering. Red and blue colors represent positive and negative values, respectively. White circles denote cycle-skipped phase travel time measurements, whereas red stars indicate travel times after cycle skipping correction (Section 4.1). The black curve illustrates the corrected phase travel time after interpolation using a grid size of 50 m. (b) Phase velocity profiles resolved for Love waves at 0.3 s underneath the 1-D linear array. White circles depict the 1-D phase velocity profile derived via eikonal equation using travel time measurements shown as the black curve in (a). The colormap illustrates phase velocity profiles obtained using different stations as virtual sources (x-axis), with white space representing the near-source exclusion zone. The phase velocity profile averaged over results of all virtual sources are depicted as red stars, with the error bar representing the corresponding standard deviation. The black vertical dashed line denotes the array-mean phase velocity estimated at 0.3 s (red star in Fig. S4b).

Figure 6. Phase velocity dispersion profiles for (a) Love and (b) Rayleigh waves beneath the RR array. The vertical dashed lines denote locations of the mapped fault surface traces (Fig. 1a), while the horizontal arrow outlines the group of stations that record fault zone trapped waves (Qin et al., 2020). Uncertainties of the resolved phase

velocity profiles are shown in (c) and (d) for Love and Rayleigh waves, respectively. Phase velocity and uncertainty profiles for Love wave at 0.4 s are excluded here due to large uncertainties (Figs. S12).

Figure 7. Comparison of (a) phase velocity and (b) uncertainty profiles of this study and those, (b) and (d), of Wang et al. (2019) in the overlapping period range. The white space indicates the area not covered by the final model. Note, the definition of phase velocity uncertainty is different in this study (standard deviation) compared to that of Wang et al. (2019) (standard deviation of the mean). A conversion is made to transform the uncertainties shown in Wang et al. (2019) into the uncertainty profiles of (d).

Figure 1.

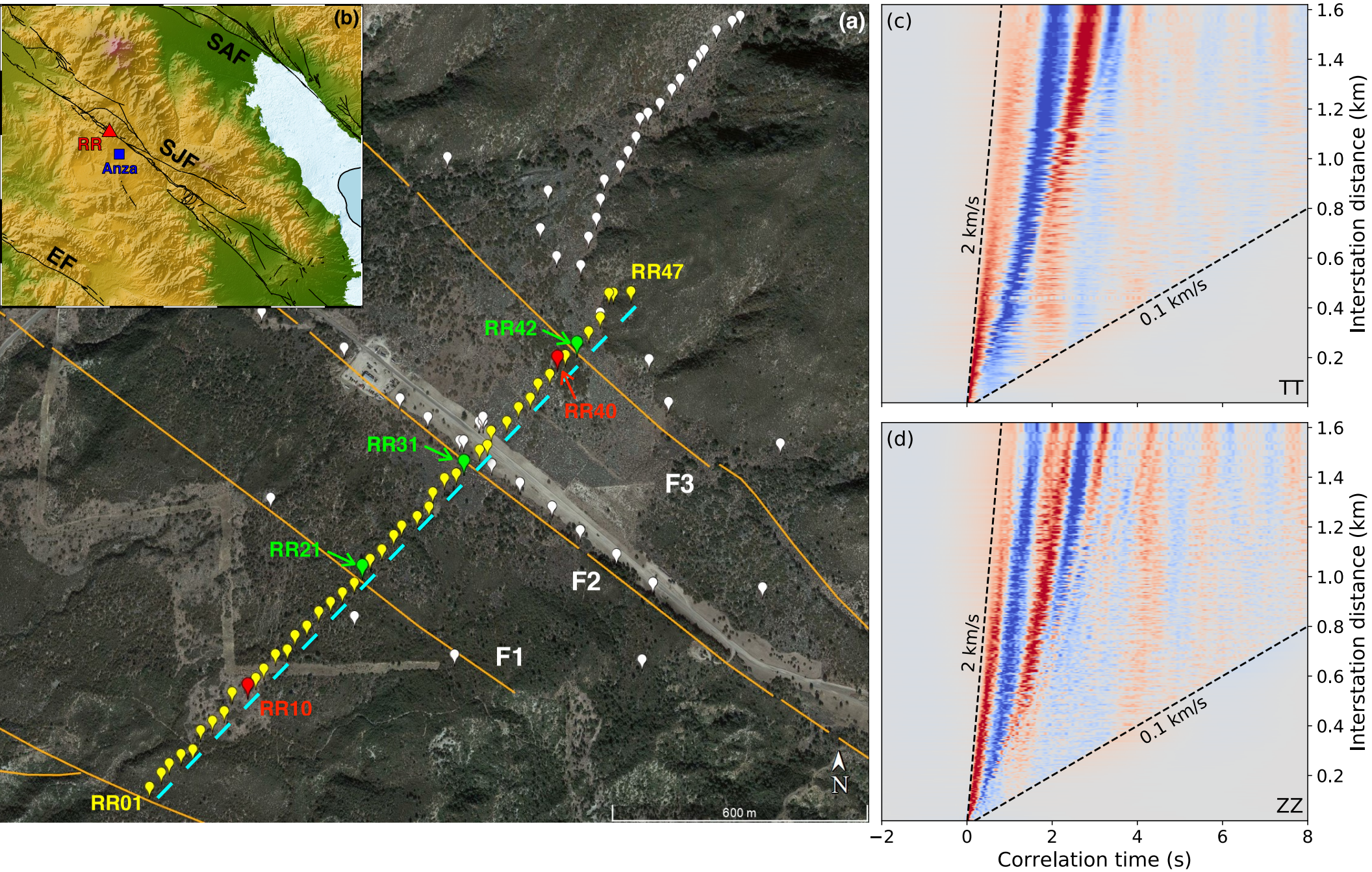
(a)
(b)
(c)
(d)
SAF
SJF
EF
RR
Anza
RR47
RR42
RR40
RR31
RR21
RR10
RR01
F1
F2
F3
N
600 m
2 km/s
0.1 km/s
TT
ZZ
Interstation distance (km)
Correlation time (s)
−2
0
2
4
6
8
0.2
0.4
0.6
0.8
1.0
1.2
1.4
1.6

Figure 2.

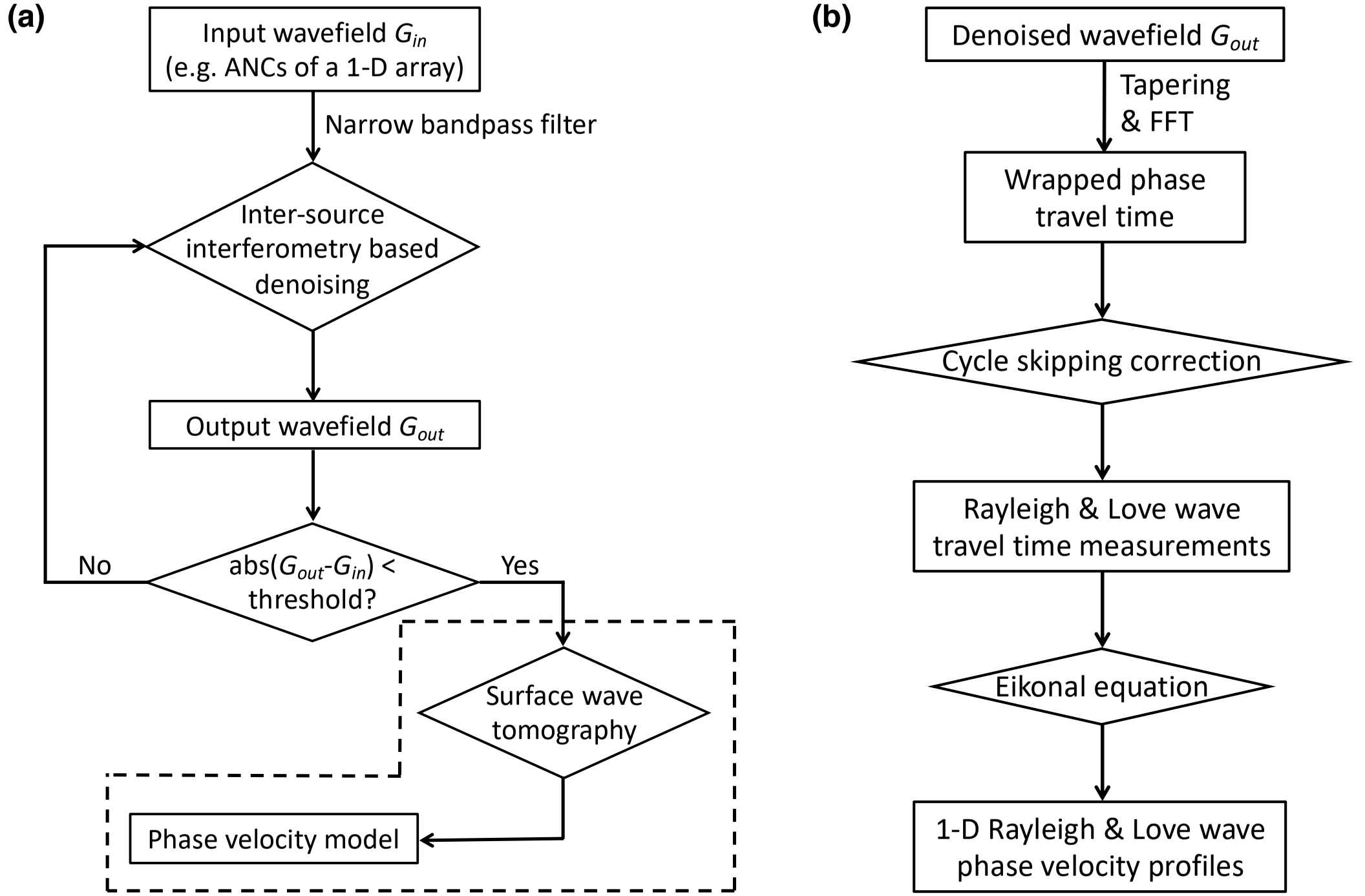
(a)
Input wavefield G_{in}
(e.g. ANCs of a 1-D array)
Narrow bandpass filter
Inter-source interferometry based denoising
Output wavefield G_{out}
abs(G_{out}-G_{in}) < threshold?
No
Yes
Surface wave tomography
Phase velocity model
(b)
Denoised wavefield G_{out}
Tapering & FFT
Wrapped phase travel time
Cycle skipping correction
Rayleigh & Love wave travel time measurements
Eikonal equation
1-D Rayleigh & Love wave phase velocity profiles

Figure 3.

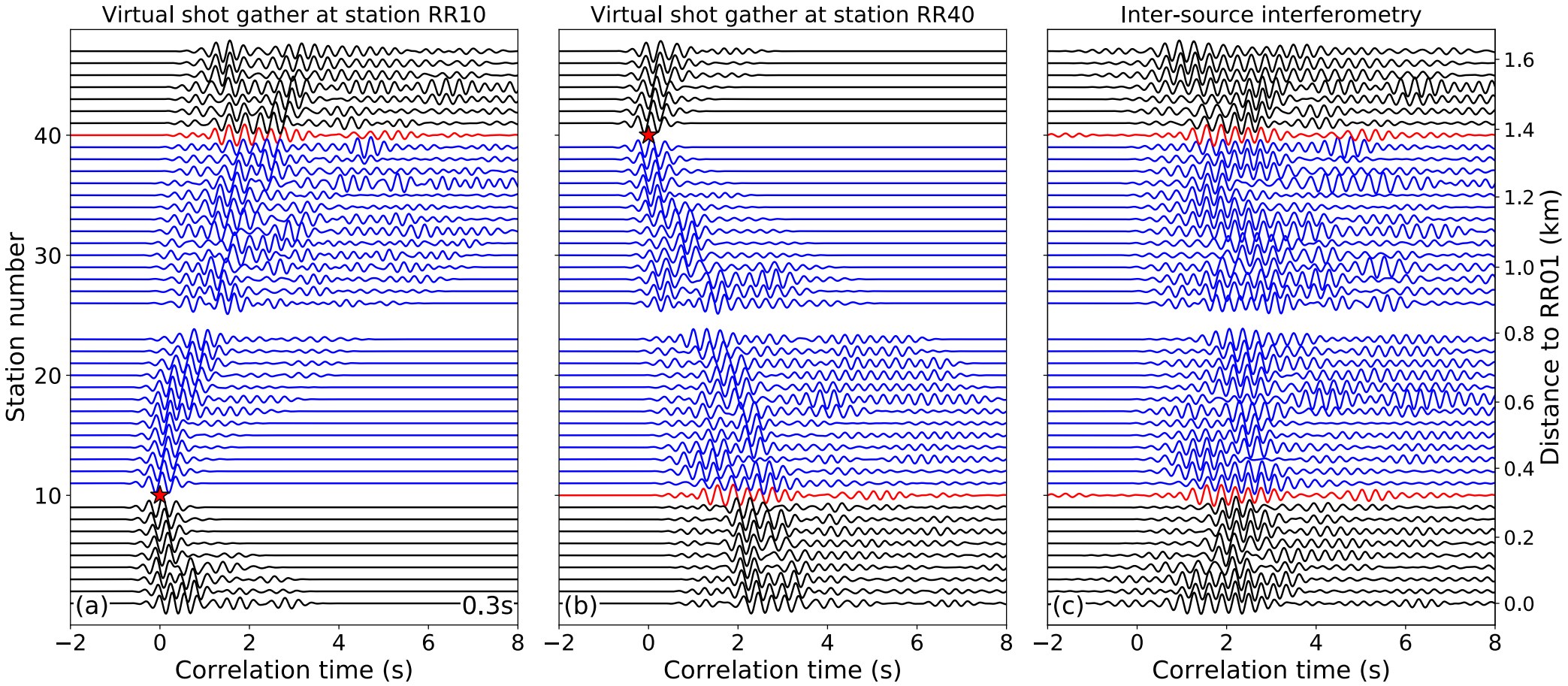
Virtual shot gather at station RR10
Virtual shot gather at station RR40
Inter-source interferometry
Station number
Distance to RR01 (km)
Correlation time (s)
Correlation time (s)
Correlation time (s)
(a)
0.3s
(b)
(c)
40
30
20
10
1.6
1.4
1.2
1.0
0.8
0.6
0.4
0.2
0.0
−2
0
2
4
6
8

Figure 4.

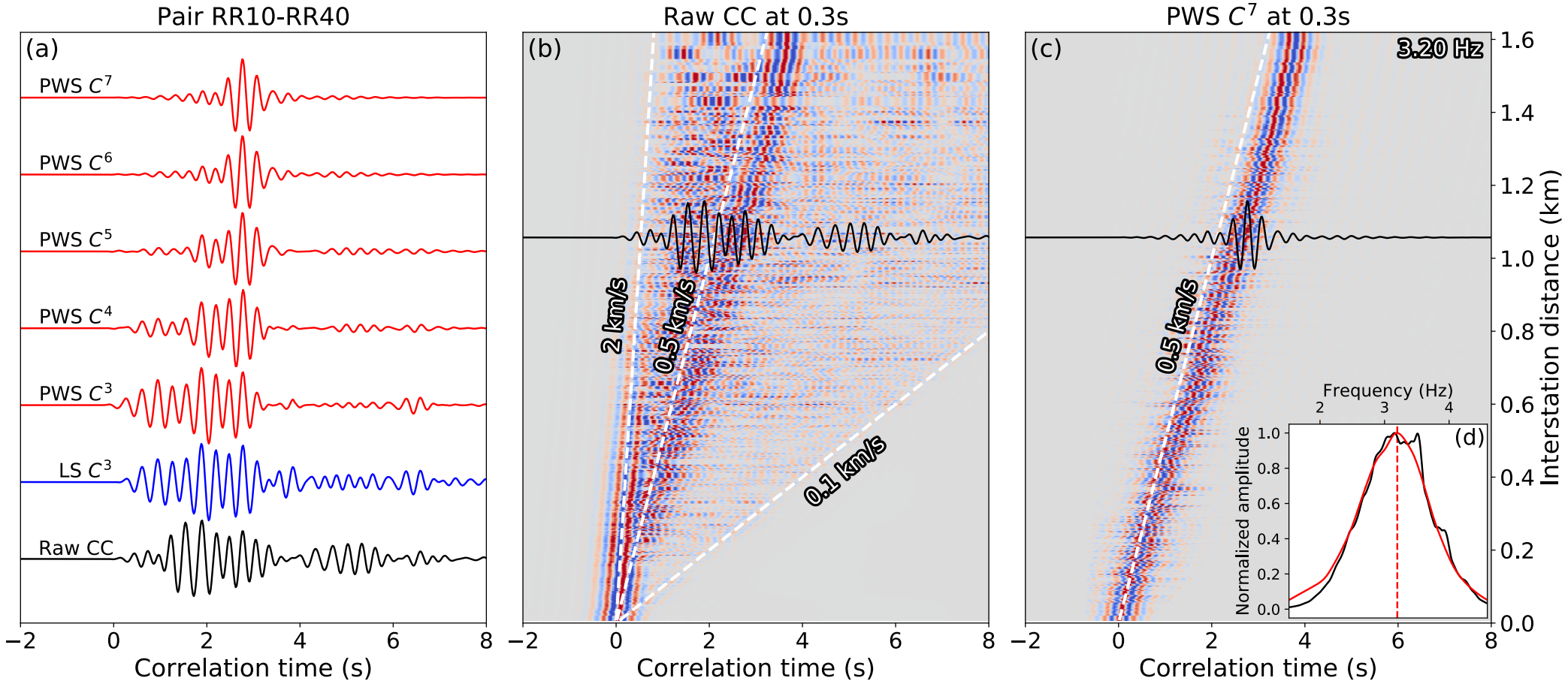
Pair RR10-RR40
(a)
PWS C^7
PWS C^6
PWS C^5
PWS C^4
PWS C^3
LS C^3
Raw CC
−2
0
2
4
6
8
Correlation time (s)
Raw CC at 0.3s
(b)
2 km/s
0.5 km/s
0.1 km/s
Correlation time (s)
PWS C^7 at 0.3s
(c)
3.20 Hz
0.5 km/s
Frequency (Hz)
(d)
Normalized amplitude
Interstation distance (km)
0.0
0.2
0.4
0.6
0.8
1.0
1.2
1.4
1.6

Figure 5.

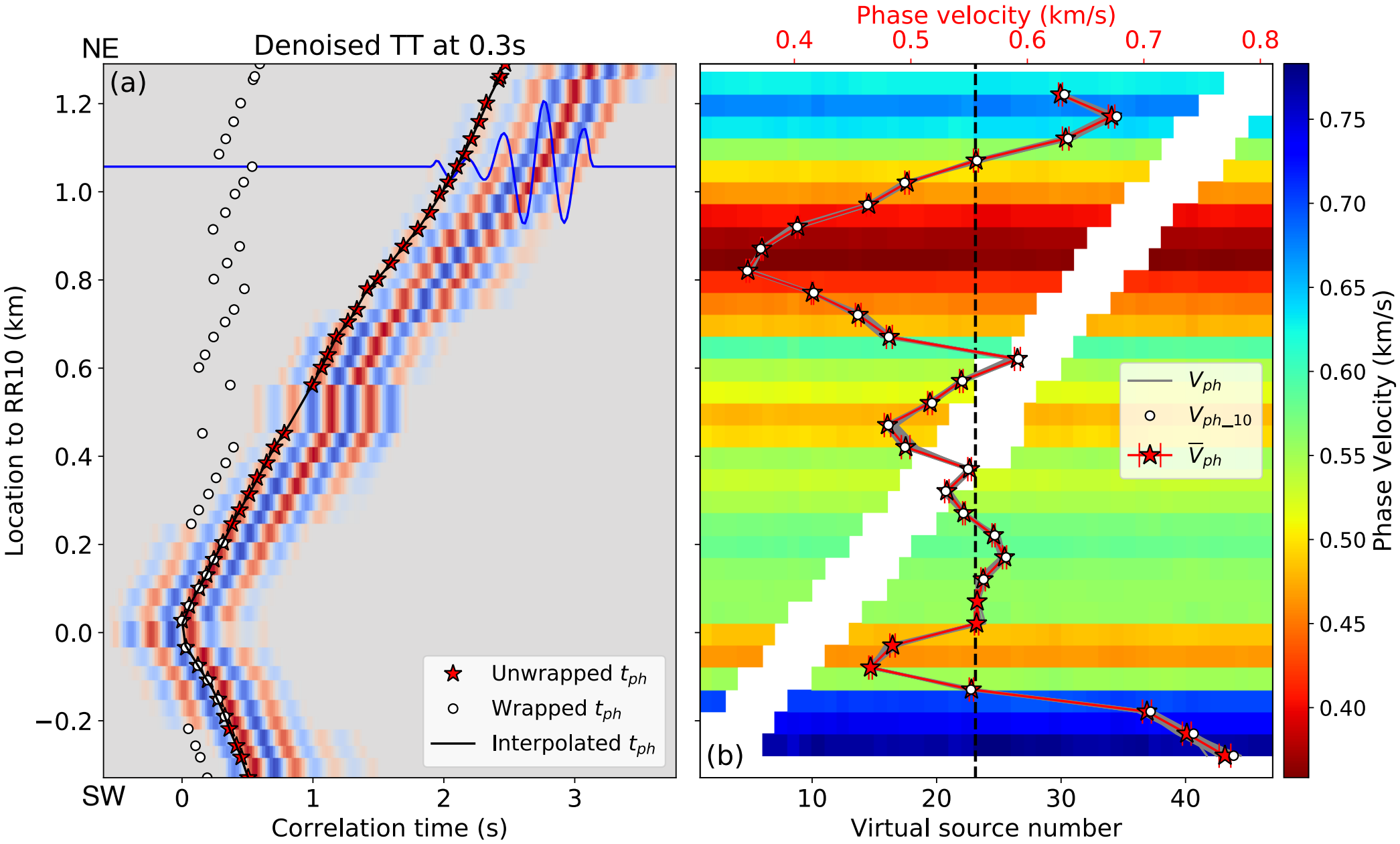
NE
Denoised TT at 0.3s
(a)
SW
Location to RR10 (km)
Correlation time (s)
Unwrapped t_{ph}
Wrapped t_{ph}
Interpolated t_{ph}
Phase velocity (km/s)
(b)
Virtual source number
V_{ph}
V_{ph_10}
$\overline{V}_{ph}$
Phase Velocity (km/s)

Figure 6.

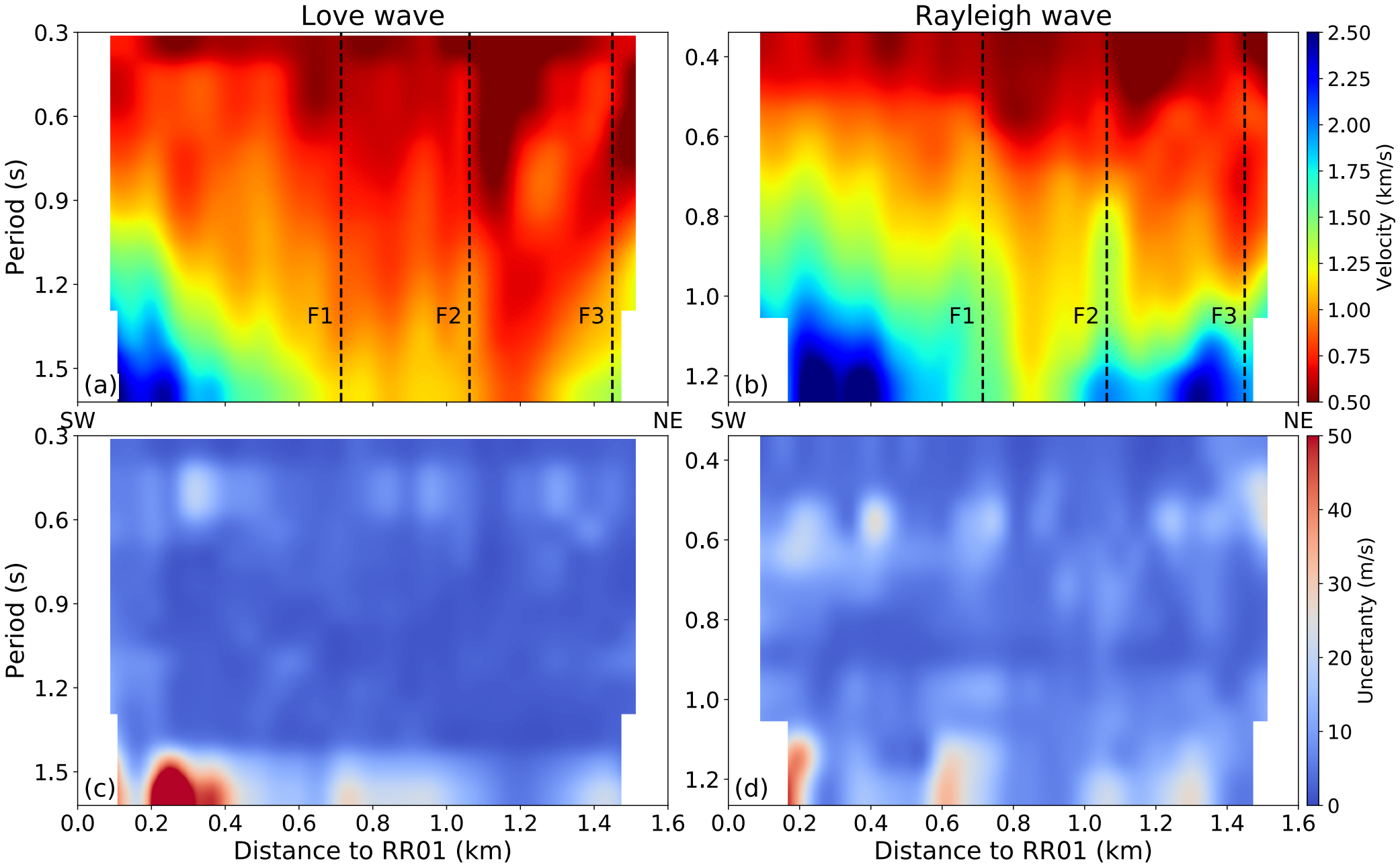
Love wave
Rayleigh wave
Period (s)
0.3
0.6
0.9
1.2
1.5
0.4
0.8
1.0
F1
F2
F3
(a)
(b)
(c)
(d)
SW
NE
2.50
2.25
2.00
1.75
1.50
1.25
1.00
0.75
0.50
Velocity (km/s)
50
40
30
20
10
0
Uncertanty (m/s)
0.0
0.2
0.4
0.6
0.8
1.0
1.2
1.4
1.6
Distance to RR01 (km)

Figure 7.

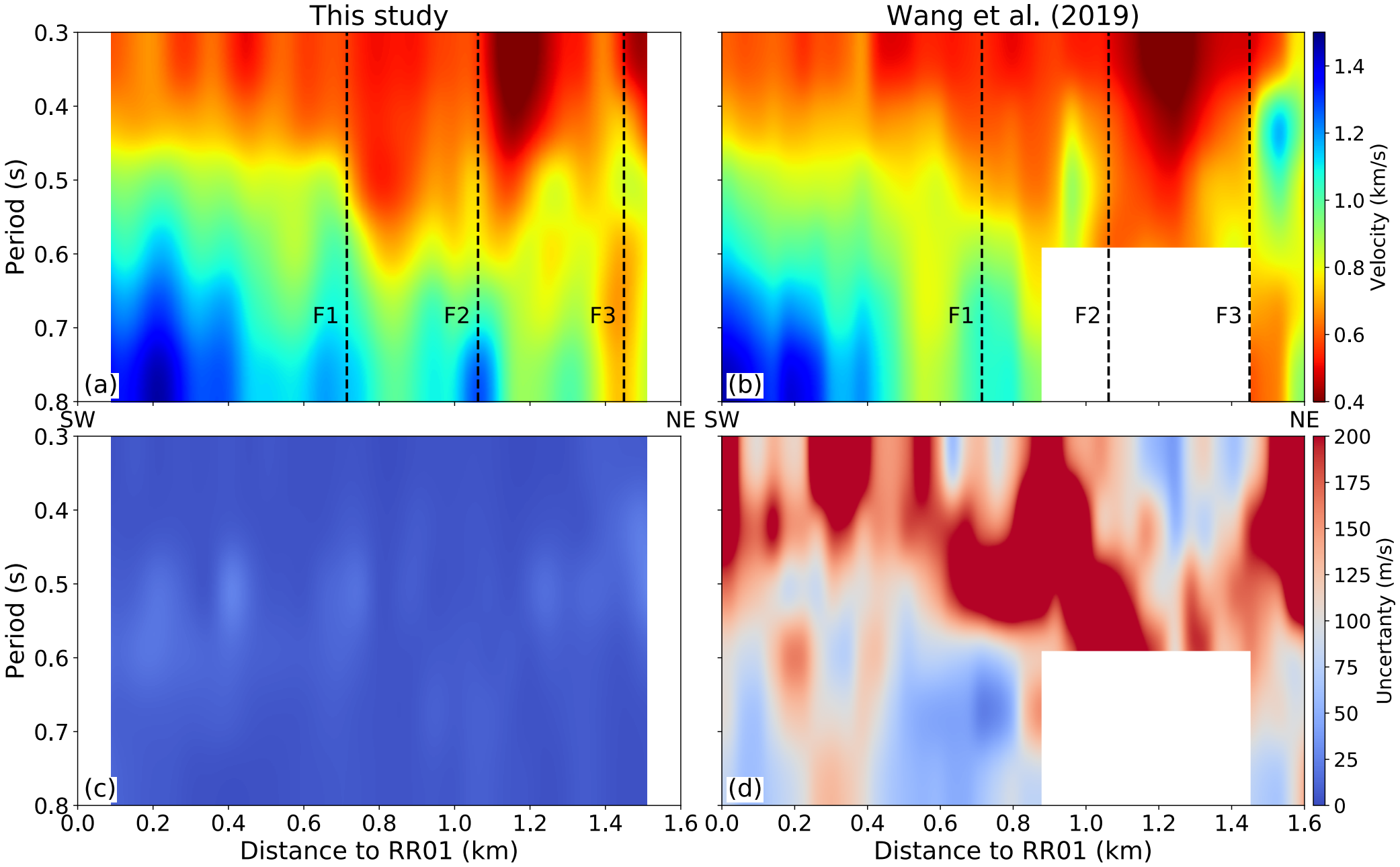
This study
Wang et al. (2019)
Period (s)
0.3
0.4
0.5
0.6
0.7
0.8
F1
F2
F3
(a)
(b)
SW
NE
Velocity (km/s)
1.4
1.2
1.0
0.8
0.6
0.4
(c)
(d)
Uncertanty (m/s)
200
175
150
125
100
75
50
25
0
0.0
0.2
0.4
0.6
0.8
1.0
1.2
1.4
1.6
Distance to RR01 (km)